



Original paper

Simulation and measurement of microbeam dose distribution in lung tissue

Gerrit Hombrink^{a,b,c}, Jan J. Wilkens^{a,b}, Stephanie E. Combs^{a,c}, Stefan Bartzsch^{a,c}^a University of Munich, School of Medicine, Klinikum rechts der Isar, Department of Radiation Oncology, Munich, Germany^b Physics Department, Technical University of Munich, Garching, Germany^c Helmholtz Centre Munich, Institute for Radiation Medicine, Munich, Germany

ARTICLE INFO

Keywords

Microbeams
Lung
Dosimetry
Monte Carlo

ABSTRACT

Microbeam radiation therapy (MRT), a so far preclinical method in radiation oncology, modulates treatment doses on a micrometre scale. MRT uses treatment fields with a few ten micrometre wide high dose regions (peaks) separated by a few hundred micrometre wide low dose regions (valleys) and was shown to spare tissue much more effectively than conventional radiation therapy at similar tumour control rates. While preclinical research focused primarily on tumours of the central nervous system, recently also lung tumours have been suggested as a potential target for MRT. This study investigates the effect of the lung microstructure, comprising air cavities of a few hundred micrometre diameter, on the microbeam dose distribution in lung. In Monte Carlo simulations different models of heterogeneous lung tissue are compared with pure water and homogeneous air–water mixtures. Experimentally, microbeam dose distributions in porous foam material with cavity sizes similar to the size of lung alveoli were measured with film dosimetry at the European Synchrotron Radiation Facility (ESRF) in Grenoble, France. Simulations and experiments show that the microstructure of the lung has a huge impact on the local doses in the microbeam fields. Locally, material inhomogeneities may change the dose by a factor of 1.7, and also average peak and valley doses substantially differ from those in homogeneous material. Our results implicate that accurate dose prediction for MRT in lung requires adequate models of the lung microstructure. Even if only average peak and valley doses are of interest, the assumption of a simple homogeneous air–water mixture is not sufficient. Since anatomic information on a micrometre scale are unavailable for clinical treatment planning, alternative methods and models have to be developed.

1. Introduction

Worldwide, lung cancer is the leading cause of cancer related death in men and second in women and made up for around 12% of new cancer cases in the year 2018 [1]. The 5 year survival ranges between 10 and 20%. Radiation Therapy is a key component of interdisciplinary treatment. However, treatment with radiation therapy is often limited, especially in patients with large volume tumors or reduced pulmonary function, as normal lung tissue is extremely radiation sensitive in terms of dose and volume. Key toxicities include pulmonary fibrosis and edema, which can lead to severe and life-threatening conditions. Therefore, treatment success with conventional radiation therapy is often poor due to this risk of severe radiation induced side effects such as pneumonitis and fibrosis [2] limiting the radiation dose to the tumour. To optimize the therapeutic window between local control optimization and reduction of side effects, alternative treatment strategies enabling better tumour control at a lower risk of severe side effects are urgently required.

A fundamentally different, but hitherto preclinical treatment strategy in radiation oncology is microbeam radiation therapy (MRT) [3] which is being developed at large third generation synchrotrons. MRT uses multiple parallel and planar, between 25 and 100 μm wide beams with a spacing of a few hundred micrometers. Microbeam peak

doses reach unconventionally high values of several hundred Gy, while the dose in the valleys between the beams remains below the tissue tolerance level. A significant body of preclinical data demonstrates that such a spatial fractionation [4] of radiotherapy doses drastically reduces the normal tissue toxicity [5–8], without compromising tumour control rate when compared to conventional radiation therapy [5,9–11].

Technical prerequisites for MRT are low photon energies of around 100keV to achieve sharp beam penumbras and a high dose rate of several 100 Gy/s to limit the effect of organ motion during the exposure. In the past preclinical research in MRT focused on brain tumours [12]. The technical rationales of the brain as target organ are comparably shallow treatment depths and little organ motion. However, due to the extraordinary tolerance of normal tissue to microbeams, MRT is a promising technique also for other tumour types and was suggested for the treatment of lung tumours [13].

Dose calculation and dosimetry in MRT is challenging due to the required high resolution and wide range of treatment relevant doses. So far, dose calculations were mostly based on Monte Carlo simulations, and carried out using various Monte Carlo codes such as EGS4 [14], EGS5 [15], PENELOPE [16] and Geant4 [17]. Many calculations assume homogeneous tissue and only a few take tissue inhomogeneities into account [16,18]. However, due to the low photon energies, material interfaces have a substantial impact on microbeam dose distribu-

tions. In the lung millions of submillimetre sized air cavities lead to a high density of water-tissue interfaces. Since the size of the alveoli of typically 50 to 250 μm have the same order of magnitude as microbeam width and spacing, it is expected that such micro-scale structures effect the microbeam dose distribution. Previous MRT dose calculations in lung have usually ignored the lung microstructure [19,20].

In this study we investigate the influence of the lung microstructure on MRT dose distributions. In a simplified model of the lung we investigate the dose absorption by means of Monte Carlo simulations. We validate these findings qualitatively with radiochromic film dosimetry in porous gels.

2. Methods

To simulate the dose distribution inside of lung tissue six different lung models (Table 1) were investigated. Model 1 consists of homogeneous material without any substructure and the chemical composition of water. It has a mean mass density of 0.26 g/cm^3 . Model 2 & 3 consist of a water filled volume with small spherical air cavities ($r = 100 \mu\text{m}$) arranged in a face centered cubic packing (fcc). The average mass density of model 2 & 3 are identical to that of model 1. For model 3 the fcc arrangement was rotated 17° around all three axes to minimize lattice effects on the dose distribution, such that the three lattice vectors pointed towards $e'_x = (0.9978 \ 0.0472 \ -0.0472)$, $e'_y = (-0.0472 \ 0.9978 \ 0.0472)$ and $e'_z = (0.0472 \ -0.0472 \ 0.9978)$. Model 4 consists of homogeneous material and the composition of water with a density of 0.54 g/cm^3 . Model 5 & 6 are set up from a water filled volume with spherical air cavities ($r = 100 \mu\text{m}$) which were arranged in a simple cubic packing, leading to the same mass density

Table 1

The table displays the six different lung models used in the Monte Carlo simulations.

Model	Density [g/cm^3]	Substructure
1	0.26	none
2	0.26	face centred cubic arrangement of air spheres
3	0.26	face centred cubic arrangement of air spheres, rotated by 17°
4	0.54	none
5	0.54	simple cubic arrangement of air spheres
6	0.54	simple cubic arrangement of air spheres, rotated by 17°

as in model 4. Similar to model 3, model 6 is rotated by 17° around all three axes.

The structures of models 1 to 6 were generated in a cubic volume of $5 \text{ mm} \times 5 \text{ mm} \times 5 \text{ mm}$ size, where energy absorption was scored. This volume was embedded into a $15 \text{ mm} \times 15 \text{ mm} \times 15 \text{ mm}$ cube of a homogeneous water-air mix with 0.26 g/cm^3 and 0.54 g/cm^3 density, respectively. Homogeneous water surrounded this artificial lung, such that the total phantom size was $25 \text{ mm} \times 25 \text{ mm} \times 25 \text{ mm}$ (see Fig. 1a). For reference purposes a simulation in which all elements of the phantom consisted of water was performed as well.

The photon source was modeled as a $20 \times 20 \text{ mm}$ radiation field of microbeams with a center-to-center distance of $400 \mu\text{m}$ and a peak width of $50 \mu\text{m}$ located 10 mm from the phantom surface. Beams were assumed to be perfectly parallel with equal beam intensity, any collimator scattering effects were neglected. The spectrum of the biomedical beamline at the European Synchrotron Radiation Facility (ESRF) with a mean photon energy of 100 keV [21] was assumed for all simulations, since the ESRF may be the facility where first clinical trials in MRT are carried out. For the models 2, 3, 5 and 6 energy absorption was scored within water only.

The resolution of the scoring grid was set to $5 \mu\text{m}$ perpendicular to the microbeams (x-axis), $250 \mu\text{m}$ parallel to the microbeams (y-axis) and $1000 \mu\text{m}$ in beam direction (z-axis). To calculate the final dose per voxel the scored energy is divided by the mean density of the corresponding voxel. The voxel densities for lung models 2, 3, 5 and 6 were approximated using Monte Carlo integration.

All Monte Carlo simulations were performed in the Geant4 toolbox version 10.0 patch 2 using the penelope physics libraries with a total number of $8 \cdot 10^9$ particle histories. The cut-off range for the simulated electrons was $1 \mu\text{m}$.

Microbeam dose distributions in porous materials were also studied experimentally by means of radiochromic film dosimetry. A bespoke PMMA phantom as displayed in Fig. 1b accommodated two different kinds of inlets, one made of gelified water (type 1) and one of a foamy water-gelatin mixture that was beaten with a household mixer (type 2). To detect short ranged secondary electrons the active layer of Gafchromic EBT3 (Ashland, USA) films was placed as close as possible to the surrounding inlet. Since the plastic protection layers before and after the active layer of the EBT3 film have a thickness of $125 \mu\text{m}$ and the range of secondary electrons for 100 keV photons have about the same free range, specially modified Gafchromic EBT3 films that lack one protection layer were used, which Ashland Inc. kindly provided.

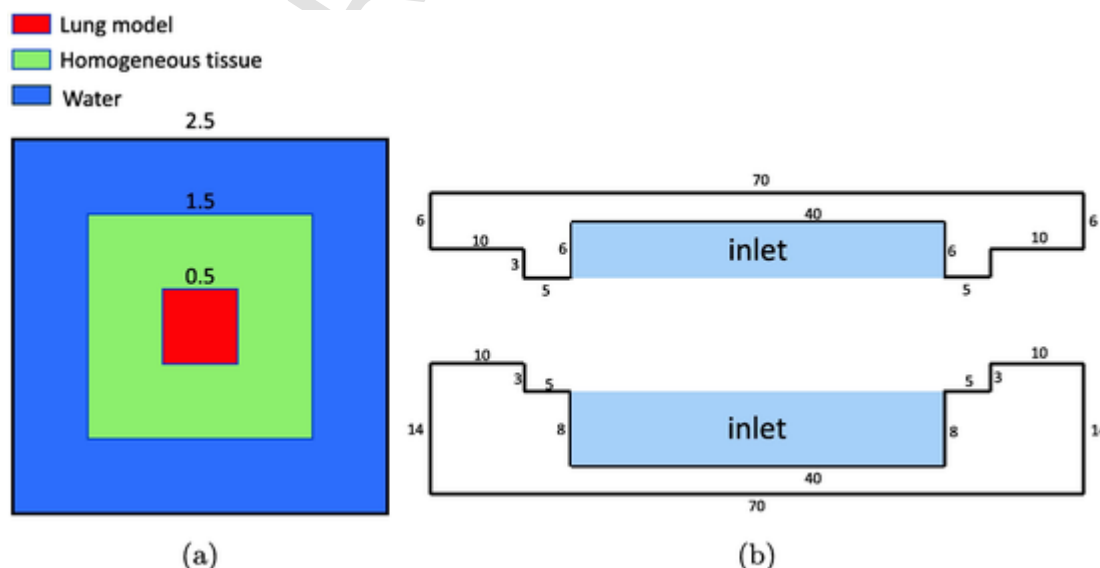


Fig. 1. (a) Displays a schematic drawing of the simulated phantom, (b) shows the phantom made of PMMA that was used for the experiment. All measures are given in mm.

Inlet type 1 is made of pure water (93 weight%) and gelatin (7 weight%) which was heated up to 50 °C under continuous stirring until the mixture changes from a milky white to clear and transparent.

After being filled into the two halves of the phantom a 6 μm thick Mylar foil is placed on top of the inlet and the phantom is cooled to 4 °C for hardening. The Mylar foil is required to prevent the inlets from sticking to the film or damaging the active layer, while keeping the distance between film and inlet as small as possible. Spare material like gel and foil were cut off with a scalpel.

For inlet type 2 again water (92.5 weight%) and gelatin (7 weight%) were mixed and heated under continuous stirring. When becoming clear and transparent 0.5 weight% of sodiumdodecylsulphate was added as a surface-active agent. The mixture was beaten with a conventional household mixer to create a firm white foam. The beating time determines the mean diameter of air cavities and was adjusted to create air cavities with a mean diameter of 115 μm and a standard deviation of 66 μm . Since the volume of the mixture increased from 100ml to around 500 ml during the beating of the foam, its density was estimated to be 0.2 g/cm³.

The experiment was performed at the ID17 beamline of the ESRF. Films were calibrated with a homogeneous field of 20 × 20 mm size. Reference dosimetry of the homogeneous radiation field was performed using a pin-point ionization chamber (PTW, PinPoint Ion Chamber 31023).

For the actual measurement the film was placed in between the two inlets before the phantom was put together. Since Gafchromic EBT3 films are sensitive in a dose range between 1 and 20 Gy [22], two films were used for the measurement, one with the peak and one with

the valley dose in the sensitive range. The evaluation of the films was performed as described previously [23].

3. Results

The simulated dose profiles were averaged along the beam axis (z-axis) and parallel to the microbeams (y-axis) and displayed in Fig. 2.

Models with internal structure showed higher peak and valley doses. In models 2 & 3 the peak dose was 18.0% and 19.1% higher than in model 1 and the valley dose increased slightly by 5.5% and 6.4%. Therefore, the PVDR of models 2 & 3 was 26.7% and 27.6% higher than in the homogeneous model 1. Also models 5 & 6 showed a 13.6% and 14.6% higher peak dose, however the increase in the valley dose was larger by 44.1% and 34.3%, respectively, leading to a reduction in PVDR of 12.5% and 5% compared to the homogeneous model 4. The comparison between water and the different lung models shows in all models except model 4 a substantial rise in valley dose of up to 60.8%.

The internal structure also changes the shape of the beam penumbras. Compared to homogeneous material of the same density the dose fall-off at the microbeam edges is steeper but becomes less steep towards the valley. To calculate the beam penumbras the distance between 10% and 90% of its peak dose was evaluated. The homogeneous model 1 showed a penumbra of 54.8 μm which is more than twice the penumbra of model 2 & 3 with 22.3 μm and 20.0 μm . A similar behaviour has been observed for model 4 with a beam penumbra of 35.0 μm compared to the penumbras of model 5 and model 6 with both 20.0 μm .

Compared to simulations in water, simulations in all of the six lung models showed a lower PVDR. The PVDR also decreased with the

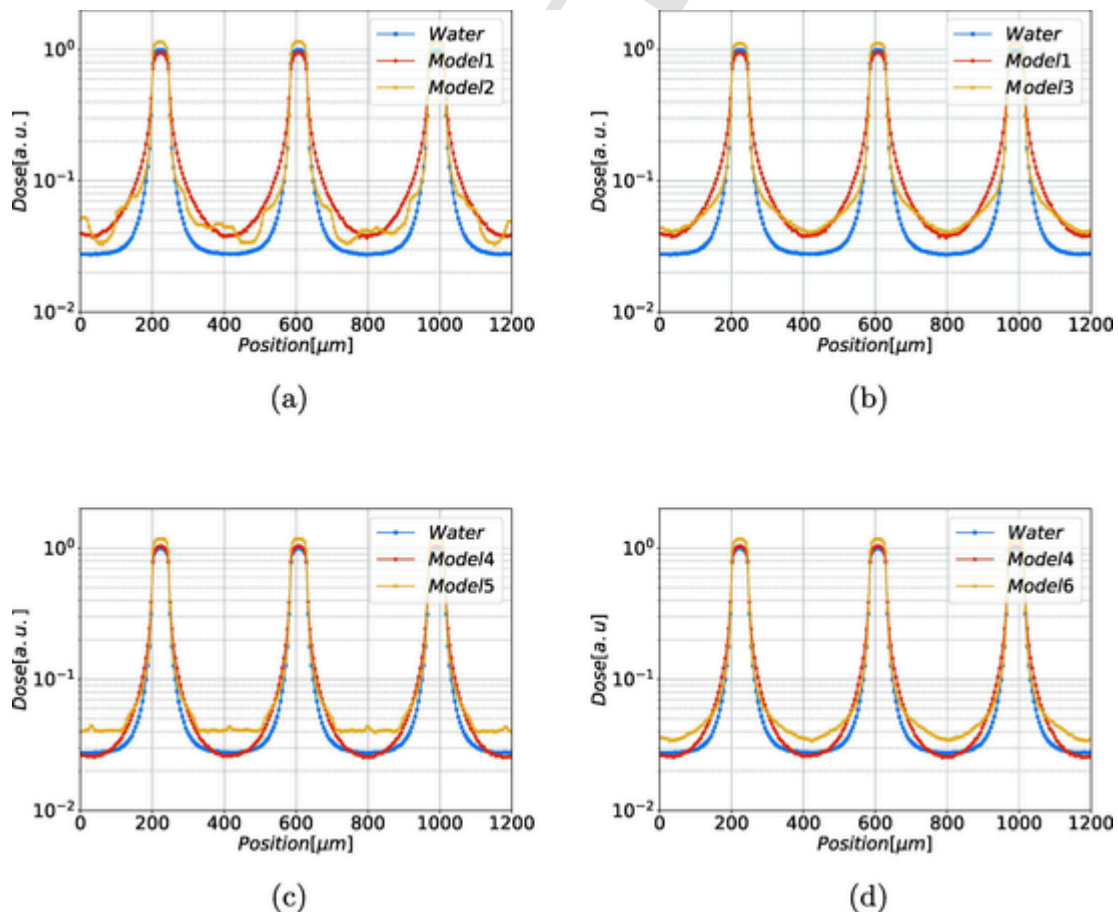


Fig. 2. (a)–(d) Display the simulations of the different lung models 2, 3, 5, and 6 in comparison to model 1 (model 4) and to water.

mean density of the absorbing medium (Fig. 3). All values are listed in Table 2.

As compared to the valley doses of models 1 and 3, model 2 showed periodically occurring inhomogeneities in the valley dose. Difference in the shape of the valley dose were also observed between models 5 and 6. The valley dose in model 5 is plateau shaped with a small peak in the middle of the valley. Model 6, however, shows a more U-shaped dose distribution.

Preparation of the gel in inlet 2 created approximately spherical air cavities of varying size. The diameter of around 300 cavities was manually measured with an optical microscope for all cavities accessible in a few randomly selected fields of views. The average air cavity diameter of the foam inlet decreased with beating time, which was set to 7 min.

Gafchromic films (Fig. 4a) that were exposed to microbeams together with inlet 2 showed up to 67% broader and more blurred peaks than those films irradiated together with inlet 1 (Fig. 4a). Furthermore, scans of films exposed with inlet 2 revealed strong variations in the valley dose while the valley dose of the films irradiated with inlet 1 was much more homogeneous. The film exposed together with inlet 2 depicts an approximately 1.5 mm diameter area in the centre of the scanned region with higher local dose. This area was situated close to a larger air cavity in the foam inlet.

4. Discussion

The Monte Carlo simulations in the lung models demonstrate that air filled micrometer sized structures in the lung tissue cause a rise of both, peak and valley doses compared to simulations without substructure. The observation of higher valley doses in model 2, 3, 5, and 6 can be explained by the strongly contrasting range of electrons in water ($140\ \mu\text{m}$ at 100 keV) and in air ($13\ \text{cm}$ at 100 keV) [24].

Compared to simulations in water, the lower mean density in the models 1 and 4 causes a higher electron range which results in electron scattering out of the peaks and subsequently wider peaks. However, due to the lower density of air, electrons can pass through the air cavities in the models 2, 3, 5, and 6 without substantial energy loss. Since the size of the cavities ($200\ \mu\text{m}$) has the same order of magnitude

as the spatial modulation of peak and valley dose, electrons from the peak regions can penetrate through the air filled areas much deeper into the valley regions than in the homogeneous models 1 and 4.

The simulations also show a strong dependence of the valley dose on the spatial arrangement of the air cavities. The largest effect is observed in model 2, where the valley dose is inhomogeneous and shows areas with higher and lower dose. The structure of the valley dose is caused by symmetry effects in the fcc cavity arrangement since the low-dose regions coincide with the position of air cavities. This effect is also visible in model 5. The plateau like shape of the valley dose and the small peak in the middle of all valley regions coincides with the position of air cavities. This effect is eliminated by rotating the arrangement in the models 3 and 6. However, it should be noted that displayed dose profiles in models 3 and 6 are averaged over volumes much larger than the cavity volume. The local energy absorption is subject to influences of nearby air cavities. In a treatment of lung tissue with microbeams, micrometer sized structures in the lung will lead to substantial local deviations from regular microbeam dose patterns. Particularly, areas close to the air-water interface will be prone to locally increased valley doses.

Due to an increase in valley dose, the PVDR decreases with smaller density as can be seen in Fig. 3. Apart from this, the lower density causes a higher electron range which enables secondary electrons to penetrate deeper into the valley region and to contribute to a higher valley dose. These two effects can be well observed in the homogeneous models 1 and 4. In the substructured models (2, 3, 5 and 6), however, the secondary electrons can pass through the air cavities without a substantial energy loss. Therefore, nearly all interactions take place in the water filled areas between the cavities leading to locally enhanced doses.

Interestingly, the effect of the microstructure on the width of beam penumbras in models 2, 3, 5 and 6 is not as clear. At the microbeam edge the dose fall-off in the structured models is as steep as in homogeneous water. In the structured models, dose is only absorbed in the water parts and there secondary electrons are shorter ranged than in the lower density materials of models 1 and 4. Consequently the mi-

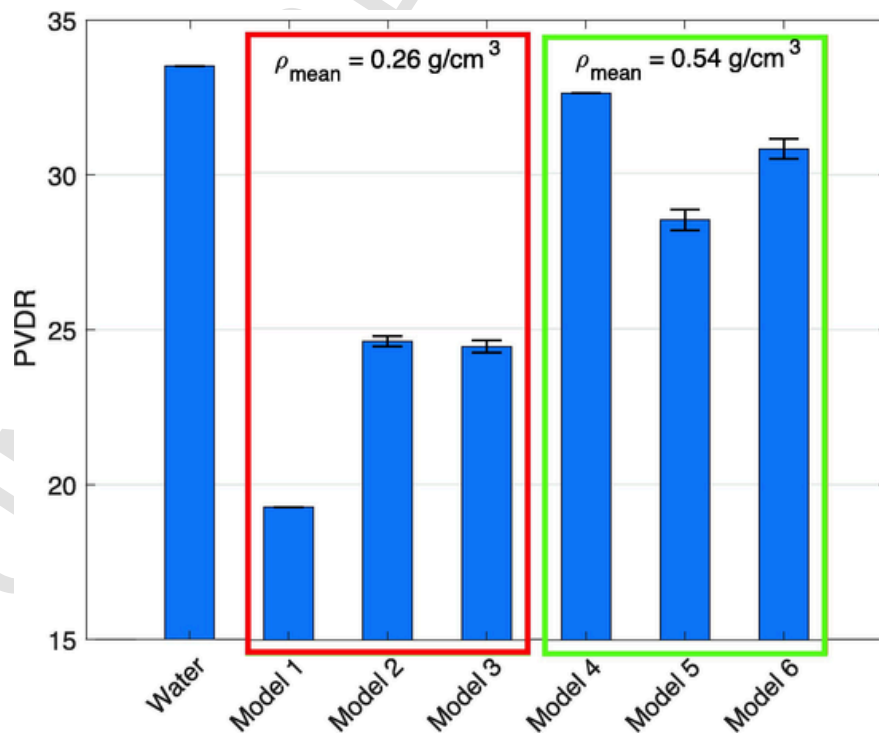


Fig. 3. The figure displays the PVDR values for all 6 lung models and water.

Table 2

The table displays peak and valley dose and the PVDR derived from the simulations. Peak and valley doses are the average dose over the central 30 μm of all peaks and central 210 μm of all valleys.

Simulation	Peak dose, normalized to water peak dose	Valley dose, normalized to water peak dose	Mean PVDR
Water	$1 \pm 0.00^*$	$(2.86 \pm 0.00^*) \cdot 10^{-2}$	$33.52 \pm 0.00^*$
Model 1	$0.94 \pm 0.00^*$	$(4.32 \pm 0.00^*) \cdot 10^{-2}$	$19.27 \pm 0.00^*$
Model 2	1.11 ± 0.01	$(4.56 \pm 0.05) \cdot 10^{-2}$	24.59 ± 0.33
Model 3	1.12 ± 0.01	$(4.60 \pm 0.05) \cdot 10^{-2}$	24.42 ± 0.32
Model 4	$1.03 \pm 0.00^*$	$(2.86 \pm 0.00^*) \cdot 10^{-2}$	$32.57 \pm 0.00^*$
Model 5	1.17 ± 0.01	$(4.12 \pm 0.02) \cdot 10^{-2}$	28.50 ± 0.17
Model 6	1.18 ± 0.01	$(3.84 \pm 0.02) \cdot 10^{-2}$	30.78 ± 0.20

*Uncertainty < 0.01.

probeam penumbras in the structured models are effectively smaller than in the unstructured models at equal average mass density. However, with distance to the microbeam edge the slope of the dose fall-off in the structured models is strongly reduced compared to the unstructured models due to air cavities allowing electrons to penetrate deep into the valley region.

The local inhomogeneities caused by air cavities were also experimentally observed as shown in Fig. 4a. The peak broadening for inlet 2 is caused by the lower density of the foam compared to the gel. This causes wider beam penumbras and larger peak widths on the film. Air cavities close to the sensitive layer cause a strong local increase in the valley dose for inlet 2.

However, the experimental data allows only a qualitative comparison due to setup uncertainties. One major obstacle for a quantitative analysis of the films is the interface between inlet and film, because small submillimeter air gaps substantially impact on the experimental results.

Both experimental and simulated results show the strong influence of micrometer sized air structures on MRT dose distribution. For pre-

cise predictions of microbeam doses in a potential future MRT treatment of the lung, the microstructure of the lung needs to be taken into account. Since structural information on the patient anatomy on such a small spatial scale is unavailable and Monte Carlo simulations involving millions of micrometer sized volumes are unrealistic, appropriate models are required that provide reasonable estimates for the therapeutically relevant peak and valley doses. The therapeutic impact of microbeam radiotherapy is large and includes the possibility of increase local control, while also reduction side effects. The present work is a solid basis for further development in microbeams towards clinical applications.

5. Conclusion

Results from experiments and simulations clearly demonstrate that the microscopic structure of alveoli and bronchioles have a substantial impact on the dose distribution when exposing lung tissue to microbeams. Both, mass density and structure strongly influence the local energy absorption. Particularly the epithelial layer will receive enhanced valley doses, since the valley dose is very sensitive to adjacent air filled cavities. Also for the prediction of average peak and valley doses the assumption of a homogeneous mixture of water and air mimicking the observed Hounsfield units of the planning CT is not sufficient.

However, detailed simulations of doses on a micrometre scale will not be feasible for clinical applications, since anatomic information on a micrometre scale are not available, and the computational load for such detailed simulations is practically not manageable. Instead, we envisage the development of analytic models that predict average peak and valley doses delivered to various tissues in the lung as a basis for a treatment related risk assessment.

Acknowledgement

We thank Ashland for providing us with Gafchromic EBT3 films without protection layer.

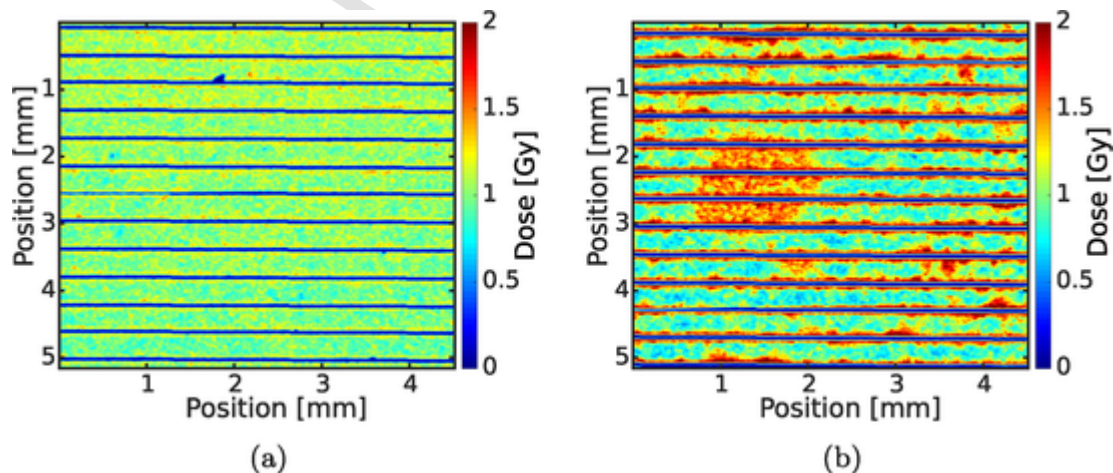


Fig. 4. (a) Displays the scanned film irradiated with inlet 1, (b) the film scan with inlet 2. The resolution was reduced to 25 μm in order to reduce the film granularity and the dose was normalized to 1 Gy mean valley dose. Please note that the peaks were outside the calibration of the films and are therefore just visualized as dark blue bars. (For interpretation of the references to color in this figure legend, the reader is referred to the web version of this article.)

References

- [1] American Cancer Society, editor. Global Cancer Facts & Figures. Atlanta: American Cancer Society, 4th edition; 2018.
- [2] Leonard L Gunderson, Joel E Tepper Clinical radiation oncology. Elsevier Health Sciences 2015.
- [3] Daniel N Slatkin, Per Spanne, F A Dilmanian, Michael Sandborg Microbeam radiation therapy. *Med Phys* 1992;19(6):1395–1400.
- [4] Elke Bräuer-Krisch, Raphaël Serduc, E A Siegbahn, Géraldine Le Duc, Yolanda Prezado, Alberto Bravin, et al. Effects of pulsed, spatially fractionated, microscopic synchrotron x-ray beams on normal and tumoral brain tissue. *Mutat Res/Rev Mutat Res* 2010;704(1–3):160–166.
- [5] Audrey Bouchet, Benjamin Lemasson, Géraldine Le Duc, Cécile Maisin, Elke Bräuer-Krisch, Erik Albert Siegbahn, et al. Preferential effect of synchrotron microbeam radiation therapy on intracerebral 9l gliosarcoma vascular networks. *Int J Radiat Oncol Biol Phys* 2010;78(5):1503–12.
- [6] Jean A Laissue, Hans Blattmann, Marco Di Michiel, Daniel N Slatkin, Nadia Lyubimova, Raphael Guzman, et al. Weanling piglet cerebellum: a surrogate for tolerance to MRT (microbeam radiation therapy) in pediatric neuro-oncology. *Proc Soc Photo-Opt Instrum Eng* 2001;4508:65–73.
- [7] Raphaël Serduc, Yohan van de Looij, Gilles Francony, Olivier Verdonck, Boudewijn van der Sanden, Jean Laissue, et al. Characterization and quantification of cerebral edema induced by synchrotron x-ray microbeam radiation therapy. *Phys Med Biol* 2008;53(5):1153.
- [8] D N Slatkin, P Spanne, F A Dilmanian, J-O Gebbers, J A Laissue Subacute neuropathological effects of microplanar beams of x-rays from a synchrotron wiggler. *Proc Natl Acad Sci USA* 1995;92(19):8783–8787.
- [9] Jean A Laissue, Gabrielle Geiser, Per O Spanne, F Avraham Dilmanian, Jan-Olaf Gebbers, Marianne Geiser, et al. Neuropathology of ablation of rat gliosarcomas and contiguous brain tissues using a microplanar beam of synchrotron-wiggler-generated x rays. *Int J Cancer* 1998;78(5):654–60.
- [10] Pierrick Regnard, Géraldine Le Duc, Elke Bräuer-Krisch, Irene Tropres, Erik Albert Siegbahn, Audrey Kusak, et al. Irradiation of intracerebral 9l gliosarcoma by a single array of microplanar x-ray beams from a synchrotron: balance between curing and sparing. *Phys Med Biol* 2008;53(4):861.
- [11] Audrey Bouchet, Elke Bräuer-Krisch, Yolanda Prezado, Michèle El Atifi, Léonid Rogalev, Céline Le Clec'h, et al. Better efficacy of synchrotron spatially microfractionated radiation therapy than uniform radiation therapy on glioma. *Int J Radiat Oncol Biol Phys* 2016;95(5):1485–94.
- [12] M A Grotzer, E Schültke, E Bräuer-Krisch, J A Laissue Microbeam radiation therapy: clinical perspectives. *Phys Med* 2015;31(6):564–567.
- [13] Michael D Wright Microbeam radiosurgery: an industrial perspective. *Phys Med* 2015;31(6):601–606.
- [14] I Orion, A B Rosenfeld, F A Dilmanian, F Telang, B Ren, Y Namito Monte carlo simulation of dose distributions from a synchrotron-produced microplanar beam array using the EGS4 code system. *Phys Med Biol* 2000;45:2497–2508.
- [15] Richard P Hugtenburg, A S Adegunloye, David A Bradley X-ray microbeam radiation therapy calculations, including polarisation effects, with the Monte Carlo code egs5. *Nucl Instrum Methods Phys Res Sec A Accelerat Spectromet Detect Assoc Equip* 2010;619(1–3):221–224.
- [16] I Martínez-Rovira, J Sempau, Y Prezado Development and commissioning of a monte carlo photon beam model for the forthcoming clinical trials in microbeam radiation therapy. *Med Phys* 2012;39(1):119–131.
- [17] Jenny Spiga, Siegbahn EA, Brauer-Krisch E, Randaccio P, Bravin A. Geant4 simulations for microbeam radiation therapy (MRT) dosimetry. In: Nuclear science symposium conference record. 2007. NSS'07, vol. 4. IEEE; 2007. p. 2571–5.
- [18] Mattia Donzelli, Elke Bräuer-Krisch, Uwe Oelfke, Jan J Wilkens, Stefan Bartzsch Hybrid dose calculation: a dose calculation algorithm for microbeam radiation therapy. *Phys Med Biol* 2018;63(4):45013.
- [19] F Z Company Calculation of dose profiles in stereotactic synchrotron microplanar beam radiotherapy in a tissue-lung phantom. *Aust Phys Eng Sci Med* 2007;30:33–41.
- [20] Banafsheh Zeinali-Rafsanjani, Mohammad Amin Mosleh-Shirazi, Mahdi Haghhigh-atafshar, Reza Jalli, Mahdi Saeedi-Moghadam. Assessment of the dose distribution of minibeam radiotherapy for lung tumors in an anthropomorphic phantom: a feasibility study. *Technol Health Care*, 2017;25(4):683–92.
- [21] Jeffrey C Crosbie, Pauline Fournier, Stefan Bartzsch, Mattia Donzelli, Iwan Cornelius, Andrew W Stevenson, et al. Energy spectra considerations for synchrotron radiotherapy trials on the ID17 bio-medical beamline at the European Synchrotron Radiation Facility. *J Synchr Radiat* 2015;22(4):1035–1041.
- [22] Gafchromic. Dosimetry media, type EBT-3. URL:http://www.gafchromic.com/documents/EBT3_Specifications.pdf.
- [23] Stefan Bartzsch, Johanna Lott, Katrin Welsch, Elke Bräuer-Krisch, Uwe Oelfke Micrometer-resolved film dosimetry using a microscope in microbeam radiation therapy. *Med Phys* 2015;42(7):4069–4079.
- [24] Berger MJ, Coursey JS, Zucker MA, Chang J. Stopping-power and range tables for electrons, protons, and helium ions. NIST standard reference database 124; 2017. URL:<https://physics.nist.gov/PhysRefData/Star/Text/method.html>.